Ab initio description of bcc iron with correlation matrix renormalization theory

Jun Liu,[1] Yongxin Yao,[1,2] Vladimir Antropov,[1,2] Kai-Ming Ho,[1,2] and Cai-Zhuang Wang[1,2]
[1]*Ames National Laboratory, Iowa State University, Ames, Iowa 50011, USA*
[2]*Department of Physics and Astronomy, Iowa State University, Ames, Iowa 50011, USA*

(Received 9 October 2023; accepted 31 January 2024; published 28 February 2024)

We applied the *ab initio* spin-polarized correlation matrix renormalization theory to the ferromagnetic state of the bulk bcc iron. We showed that it was capable of reproducing the equilibrium physical properties and the pressure-volume curve in good comparison with experiments. We then focused on the analysis of its local electronic correlations. By exploiting different local fluctuation-related physical quantities as measures of electronic correlation within target orbits, we elucidated the different roles of t_{2g} and e_g states in both spin channels and presented compelling evidence to showcase this distinction in their electronic correlation.

DOI: 10.1103/PhysRevB.109.085147

I. INTRODUCTION

Iron, a prototypical magnetic material, is integral to our daily lives. Experimental studies have ascertained that its low-temperature ground state, the α-Fe phase, exhibits a bcc crystal structure with an equilibrium lattice volume of 11.7 Å^3 (equivalent to lattice constant $a = 2.86$ Å) and a bulk modulus of 168 GPa [1]. As a ferromagnetic substance, it possesses an ordered spin magnetic moment of 2.13 μ_B and orbital magnetic moment of 0.08 μ_B [2]. The system displays discernible electronic correlation. Specifically, an effective local Hubbard interaction U for $3d$ electrons in iron has been identified within a range of $\sim 1-3$ eV and a definitive ratio of $U/W \simeq 0.2$ was established, with W representing the bandwidth of $3d$ states [3–5]. This observation was later corroborated by a theoretical study coming up with a close U/W ratio [6]. Such characteristics were further evidenced in various experimental outcomes that diverge from their mean-field-like theoretical predictions and interpretations [4,7]. Presently, both experimental and theoretical efforts have categorized α-Fe as a local moment system with a great tendency towards itinerancy [8]. But a consensus is yet to be reached on the underlying physical mechanism on the formation of the strong ferromagnetism in α-Fe [9–12].

Density functional theory (DFT) [13], including local spin density approximation (LSDA) [14,15] and its generalized gradient approximation (GGA) [16], has been applied to α-Fe to understand its peculiar physical properties from a microscopic perspective. LSDA's predictions deviated from experimental findings and suggested a notably reduced equilibrium lattice constant for the ferromagnetic ground state of α-Fe [17]. Adjusting this discrepancy involves enhancing the kinetic energy via nonlocal charge density variations and employing compatible exchange-correlation functionals akin to GGA, for instance, the Perdew-Burke-Ernzerhof (PBE) functional [18]. These modifications yielded commendably accurate depictions concerning the right ferromagnetic ground state and its innate properties [10,19]. Broadly, DFT furnishes a reasonable portrayal of α-Fe, including its energy ground state and quasiparticle characteristics [19–21]. Specifically, it validates the Stoner mechanism for the emergence of spontaneous ferromagnetism in bcc Fe [22]. Other weakly interacting techniques, for example, the GW approximation [23] and quasiparticle self-consistent GW (QSGW) [24,25], have also been applied to the system, purporting enhanced efficacy relative to GGA. A semi–*ab initio* Hartree-Fock (HF) calculation, where local and nonlocal interaction operators were separately scaled, was also reported to have produced a quite consistent band structure as DFT [26]. Nevertheless, there is room for further refinement to illuminate the subtle aspects of α-Fe such as local moment formation and competition between localized and itinerant electrons, and to bridge the gap between theory and experiments, notably through addressing both local and nonlocal electronic correlations [25,27–30].

Advanced *ab initio* techniques, specifically designed to treat local electronic correlation, have been employed to investigate the bcc iron system. Notable methods included LDA + U [31], LDA + dynamic mean-field theory (LDA + DMFT) [9,28,32,33] and LDA + Gutzwiller (LDA + G) [34–36]. While LDA + DMFT is considered the state-of-the-art *ab initio* method, it is also computationally demanding. It was shown to improve the agreement between theory and experiment, including very subtle aspects of quasiparticle properties such as broadening of quasiparticle spectra [33], local spin splitting [9,32], and the emergence of satellite subband [37]. Specifically, it gave numerical evidence of the distinct nature of the t_{2g} and e_g states in electronic [9] as well as magnetic [38] contexts, and ascribed the local moment mainly to e_g electrons [9]. LDA + G can be regarded as a simplified and accelerated version of LDA + DMFT with a different definition of the Baym-Kadanoff functional within the conserving approximation [39]. It made specific physical observations based on its output and produced information on quasiparticle dispersion. The engaged treatment of local electronic interactions helped introduce new interpretations of ferromagnetism from DFT methods [34]. However, the

notable challenge with these methods is the variability in defining the effective Hubbard U and exchange J parameters. These parameters are essential for outlining screened local electronic interactions. They could differ significantly across separate implementations and were often calibrated to align with certain experimental data [27,30,34–36]. Specifically, the U value can range from 2 to 9 eV, and J between 0.5 and 1.2 eV, a considerable spread for similar *ab initio* techniques. Nevertheless, there were reassuring studies indicating that magnetic properties are more influenced by J than U [27,36].

DFT and its embedding methods, including LDA + U, LDA + G, and LDA + DMFT mentioned above, enriched our knowledge for a better understanding of the microscopic origin of the ferromagnetism in the bulk bcc iron system by analyzing physical quantities coming out of the calculations and confirmed the importance of the role local electronic correlation plays in producing a more accurate theory to meet experiments. Local physical quantities that have been analyzed include local self-energy, spectral function, spin-spin susceptibilities [9,28], local orbit occupation and mass renormalization factor [34], local charge (spin) distribution [36], etc. They have provided direct evidence of the existence of local moment, asymmetry between t_{2g} and e_g states, and notable influence from electronic correlation. In this work, we aim to delve deeper into some of these subjects, employing data from the recently introduced *ab initio* method, i.e., correlation matrix renormalization theory (CMRT) [40–42]. Uniquely, CMRT utilizes Hartree-Fock (HF) rather than DFT for the foundational single-particle effective Hamiltonian. A strength of integrating HF into CMRT is its direct engagement with termwise bare Coulomb interactions, eliminating the need for adjustable U, J energy parameters and double-counting choices, and avoiding self-interaction complications. However, this approach also has drawbacks: HF offers a less realistic quasiparticle foundation for CMRT. Therefore, ensuring that the many-body screening effects are properly incorporated within CMRT is essential. We thus assessed the total energy of the system and compared the derived pressure-volume curve to experimental data to ensure they are closely aligned, a necessary step for CMRT to proceed further. We then devised a series of correlation metrics to tell the distinct roles of the t_{2g} and e_g states across spin channels.

In what follows, we will distinguish local density approximation (LDA) from LSDA, with the former spin unpolarized and the latter spin polarized, while for the other methods mentioned, such as HF, LDA + G, LDA + U, LDA + DMFT, and CMRT, they all refer to the spin-polarized calculations.

II. METHODS

CMRT is a fully *ab initio* variational theory specifically tailored for strongly correlated electron systems utilizing a multiband Gutzwiller wave function as its trial state [41]. Notably, in the context of transition-metal systems, CMRT offers a cohesive framework that accommodates both itinerant and localized electrons within the same electronic structure calculation, akin to DFT-embedded correlated *ab initio* methodologies [34].

For a periodic bulk system with one atom per unit cell, the CMRT ground-state total energy is

$$E_{\text{total}} = \sum_{\substack{ij\\ \alpha\beta,\sigma}} \tilde{t}_{i\alpha,j\beta;\sigma} \langle c^\dagger_{i\alpha\sigma} c_{j\beta\sigma} \rangle + \frac{1}{2} \times \sum_{\substack{ijkl\\ \alpha\beta\gamma\delta,\sigma\sigma'}} \tilde{U}^{\alpha\beta\gamma\delta}_{ijkl;\sigma\sigma'} (\langle c^\dagger_{i\alpha\sigma} c_{k\gamma\sigma} \rangle \langle c^\dagger_{j\beta\sigma'} c_{l\delta\sigma'} \rangle - \delta_{\sigma\sigma'} \langle c^\dagger_{i\alpha\sigma} c_{l\delta\sigma'} \rangle \langle c^\dagger_{j\beta\sigma'} c_{k\gamma\sigma} \rangle) + E_{\text{local}}, \tag{1}$$

with the local energy E_{local} expressed as

$$E_{\text{local}} = \sum_i \sum_\Gamma \tilde{E}_{i\Gamma} (p_{i\Gamma} - p_{i\Gamma_0}), \tag{2}$$

and the dressed hopping and two-body interactions defined as

$$\tilde{t}_{i\alpha,j\beta;\sigma} = t_{i\alpha,j\beta} + \frac{N_e}{2} \lambda^{\alpha\beta\beta\alpha}_{ijji;\sigma\sigma}, \tag{3}$$

$$\tilde{U}^{\alpha\beta\gamma\delta}_{ijkl;\sigma\sigma'} = U^{\alpha\beta\gamma\delta}_{ijkl} - \lambda^{\alpha\beta\gamma\delta}_{ijkl;\sigma\sigma'}. \tag{4}$$

Here, i, j, k, l represent site indices, $\alpha, \beta, \gamma, \delta$ are orbital indices, and σ, σ' correspond to spin indices. Γ denotes Fock states in the occupation number representation of local correlated orbitals on each atom in the unit cell, while N_e is the system's electron count per unit cell. The energy parameters $t_{i\alpha,j\beta}$ and $U^{\alpha\beta\gamma\delta}_{ijkl}$ are the bare hopping and Coulomb integrals, respectively. The sum rule correction coefficient $\lambda^{\alpha\beta\gamma\delta}_{ijkl;\sigma\sigma'}$ is introduced in CMRT to specifically enhance the accuracy of the total-energy calculation. $\tilde{E}_{i\Gamma}$ are the Fock state eigenvalues of the dressed local correlated Hamiltonian on each site.

The initial two terms in Eq. (1) yield the expectation value of the dressed lattice Hamiltonian under CMRT, where the expectation values of two-body operators expand following Wick's theorem in terms of one-particle density matrices, which is defined as

$$\langle c^\dagger_{i\alpha\sigma} c_{i\beta\sigma} \rangle = f(z_{\alpha\sigma}) f(z_{\beta\sigma}) \langle c^\dagger_{i\alpha\sigma} c_{i\beta\sigma} \rangle_0 + [1 - \delta_{\alpha\beta} f^2(z_{\alpha\sigma})] \bar{n}_{i\alpha\sigma}. \tag{5}$$

Here, $z_{\alpha\sigma}$ represents the Gutzwiller renormalization factor, while $\langle\cdot\rangle_0$ indicates the one-particle noninteracting density matrix and $\bar{n}_{i\alpha\sigma}$ the local electronic occupation of state α. The function $f(z_{\alpha\sigma})$ is integrated to ensure CMRT aligns with the solution of an exactly solvable model [42] under certain conditions. The third term in Eq. (1) is essential for preserving dominant local physics in CMRT by rigorously expressing the local correlated energy through the variational parameter $p_{i\Gamma}$, which denotes the occupational probability of Fock state Γ spanned by the correlated atomic orbits at site i. The noninteracting counterpart, $p_{i\Gamma_0}$, denotes the same quantity evaluated with the mean-field approximation and correlates with the local energy components already assessed in the initial two terms of Eq. (1). The underlying local correlated Hamiltonian behind the third energy term of Eq. (1) encompasses primary two-body Hubbard-type Coulomb interaction terms dominating local spin and charge interactions. Its exact treatment particularly helps preserve intrinsic local spin

and charge fluctuation effects and generate local magnetic moments. The Hund's coupling exchange interaction terms, which are believed to be physically relevant for bcc iron [9,27], are approached in a mean-field way in CMRT.

The sum rule correction coefficients, provisionally represented as

$$\lambda^{\alpha\beta\gamma\delta}_{ijkl;\sigma\sigma'} = \lambda^{\alpha}_{i\sigma}\delta_{ik}\delta_{jl}(1-\delta_{ij})\delta_{\alpha\gamma}\delta_{\beta\delta}, \tag{6}$$

are integrated explicitly into CMRT to aid in counteracting errors associated with the Fock terms in Eq. (1), a significant error source of CMRT. The sum rule correction coefficients serve to redistribute nonlocal Coulomb interactions onto local sites, thus further refining the total energy by exactly treating these local interactions. The central term $\lambda^{\alpha}_{i\sigma}$ in Eq. (6) for each correlated orbit is tested out in this work for magnetic systems. Its optimal functional form is determined following the logic of cancellation of intersite Fock contributions and is identified as

$$\lambda^{\alpha}_{i} = \frac{\sum_{\sigma'}\left[\sum_{j\neq i}\sum_{\beta} U^{\alpha\beta\alpha\beta}_{ijij}|\langle c^{\dagger}_{i\alpha,\sigma'}c_{j\beta,\sigma'}\rangle|^2\right]}{\sum_{\sigma'}\left[\sum_{j\neq i}\sum_{\beta}|\langle c^{\dagger}_{i\alpha,\sigma'}c_{j\beta,\sigma'}\rangle|^2\right]}. \tag{7}$$

One reassuring aspect of the above definition is the spin-independent nature of the term, which aligns with the system's bare *ab initio* Hamiltonian. There, the energy coefficients of one-body and two-body operators are all spin independent. Thus, whatever magnetization is produced in CMRT is a genuine characteristic of the system, but not endowed by certain predefined energy parameters.

The variational minimization of the CMRT total energy, as given by Eq. (1), yields a set of Gutzwiller equations [41]. These equations are self-consistently solved to reach the optimal solution for the target system. For weakly correlated lattice systems, the volume-dependent total energy and related physical quantities produced by CMRT have been found to align closely with experimental results [41]. In the realm of strongly correlated systems, CMRT has demonstrated its prowess in capturing the correlated nature of $4f$ electrons in fcc Ce and fcc Pr [43,44]. By interfacing with the Hartree-Fock (HF) module of the Vienna Ab Initio Simulation Package (VASP) [45], CMRT has been efficiently implemented with the quasi-atomic minimal basis set orbitals (QUAMBO) basis set [46], and its computational speed mirrors that of a minimal basis HF calculation [41,44]. While still less speedy than LDA + G, such a CMRT calculation marks a significant performance gain over the more time-consuming quantum Monte Carlo (QMC) methods, or LDA + DMFT when QMC is used as its impurity solver. Specifically, for this work, a complete plane-wave basis set setting up the VASP working environment was defined with the default energy cutoff prescribed by the pseudopotential of Fe. Brillouin zone sampling was facilitated with VASP using an automatically generated K-point grid maintaining a R_k length of 40 ($R_k = 40$), which amounts to a $20 \times 20 \times 20$ uniform mesh at the experimental lattice constant. The local QUAMBO minimal basis set of $3d4s4p$ states for CMRT to work with are projected from a set of LDA Kohn-Sham eigenstates preserving the low-energy spectrum up to 1 eV above the LDA Fermi energy. These spin-independent localized orbits define the tight-binding Hamiltonian and the bare Coulomb interactions and thus preserve the spin symmetry of the Hamiltonian.

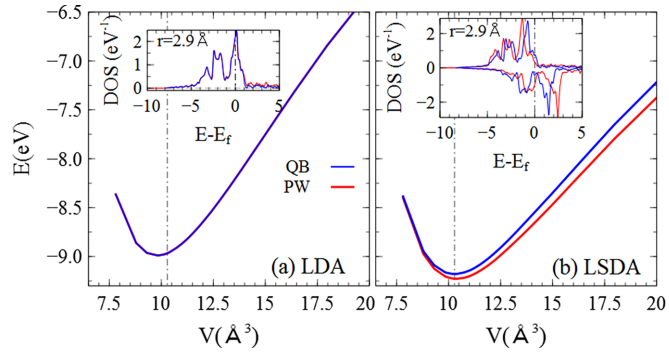

FIG. 1. Comparison of LDA and LSDA total energies for bcc iron between using a complete plane-wave basis set and using the QUAMBO minimum basis set projected from LDA eigenstates. Insets show the DOS from all the calculations evaluated at a lattice constant of $r = 2.9$ Å. Curves in blue refer to the QUAMBO basis set and curves in red refer to the plane-wave basis set.

It is imperative to note that our CMRT utilized the QUAMBO local basis set, which, although not complete, stands out as the most efficient minimal basis set for reproducing all low-lying KS states up to a few eV above the Fermi level, as corroborated by the performance comparison against a more extensive plane-wave basis set in Fig. 1. The QUAMBO basis set, derived from a select range of LDA eigenstates computed using a comprehensive plane-wave basis set, inherently replicates the LDA results, as depicted in Fig. 1(a). While such a replication does not extend to LSDA calculations by default, the agreement between the two basis sets is still quite impressive, as shown in Fig. 1(b). There, the QUAMBO-based LSDA calculation yields a slightly elevated total energy compared to its plane-wave counterpart, a discrepancy aligning with differences in basis set sizes. Notwithstanding this, both approaches yield quite similar results in terms of equilibrium lattice constants and bulk moduli. The inset of the figure showcases the density of states (DOS) produced by the two methods. It reveals an almost indistinguishable DOS for the LDA calculations across both basis sets within the prescribed energy window. Intriguingly, the QUAMBO application in the LSDA calculations demonstrates a significant enhancement in the spin gap, which is quite unforeseen yet surely noteworthy.

III. RESULTS

A. Total energy and its related physical quantities

In the study of the ferromagnetic ground state of the bulk bcc Fe lattice, energy versus volume (E-V) curves are collected and compared in Figs. 2(a) and 2(b). These curves contain results from several calculation methods, including HF, LSDA, GGA(PBE), LDA + U, LDA + G, LDA + DMFT, and CMRT. Both HF and CMRT calculations share the same QUAMBO basis set, while LSDA, GGA(PBE), and LDA + U are evaluated with the plane-wave basis set. The rest are published results. The GGA data are cross checked against Ref. [19]. To complement the E-V curves, the pressure

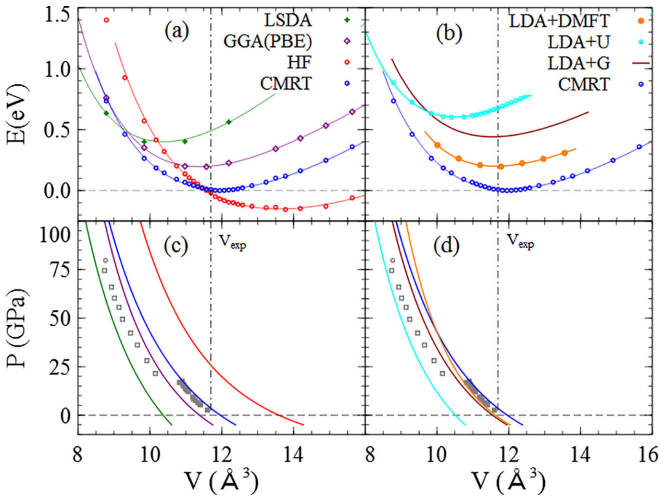

FIG. 2. Energy vs volume (E-V) and pressure vs volume (P-V) curves for ferromagnetic bcc iron calculated with different *ab initio* methods. (a) Comparison of CMRT against weakly interacting methods including LSDA, GGA(PBE), and HF. (b) Compilation of strongly correlated methods, including LDA + DMFT ($U = 4.3$ eV, $J = 1.0$ eV) [29], LDA + U ($U = 2.2$ eV, $J = 1.0$ eV), LDA + G ($U = 7.0$ eV, $J = 1.0$ eV) [35], and CMRT. The corresponding P-V curves are depicted in solid lines in (c) and (d). LSDA, PBE, and LDA + U are evaluated with VASP at an automatic K grid of $R_k = 40$. HF used the identical QUAMBO basis set and K grid as CMRT. Experimental measurements are symbolized as follows: solid squares for bcc α-Fe phase and empty squares for hcp ε-Fe phase [19,48]. Vertical adjustments have been made for all the energy curves for a clearer view. Specifically, HF energy is downshifted an extra 5.5 eV with respect to CMRT energy in the figure. Vertical dash-dotted lines mark the experimental equilibrium volume of the ferromagnetic bcc Fe lattice.

versus volume (P-V) curves were extracted from their Birch-Murnaghan equation of state (BM-EOS) [47] fits and were also showcased in Figs. 2(c) and 2(d), side by side with the experimental measurements. The accompanying fitted equilibrium volumes and bulk moduli as well as the calculated magnetic moments and their pressure derivative are collected in Table I. Note that the $U = 4.3$ eV, $J = 1.0$ eV values used in the LDA + DMFT calculation was chosen to match the experimental spin magnetic moment value of 2.2 μ_B at $T =$ 290 K [29]. Meanwhile, there were varied parameter choices for LDA + G in the literature; here it uses $U = 7.0$ eV and $J = 1.0$ eV [29]. By examining the intersection points of these curves with the volume axis, we can discern the distribution of equilibrium volumes for each method in relation to the experimental volume. This provides a clear view of the exemplary performance of both the GGA and CMRT methods, which operate without the need for adjustable energy parameters, and commendable outcomes of LDA + G and LDA + DMFT with appropriate U, J energy parameters used for the calculations. The alignment between the CMRT-generated data and experimental pressure-volume measurements stands out. Specifically, CMRT demonstrates a closer resemblance to experimental outcomes for the bcc iron phase when compared to GGA.

One might wonder how local energy corrections resulting from electronic correlations might influence the total energy in CMRT calculations. This particular contribution is encapsulated in E_{local} as seen in Eq. (1). As described by Eq. (2), E_{local} encompasses predominant energy terms arising from the $\hat{n}_{i\alpha,\sigma}\hat{n}_{i\beta,\sigma'}$ type of two-body operators, where α and β represent the set of local correlated orbits. This term delineates the discrepancy between the strict expectation values and their corresponding mean-field values. Typically, each term in E_{local} is negative, reflecting diminished Coulomb interaction stemming from the presence of local electronic repulsion. We have assigned an additional negative sign to these terms for a clearer visualization in Fig. 3. A general understanding might suggest that local correlation energy gain amplifies with increasing volume expansion. Yet, contrary to this notion, the inset of the figure displays a different trend. The root of this behavior can be traced back to the terms that most significantly influence E_{local}, as exemplified at three distinct volumes across the experimental equilibrium volume. These individual energy terms are segregated into separate spin-spin channels on the x axis of Fig. 3: $\uparrow\uparrow$ for majority-majority spin, $\uparrow\downarrow$ for majority-minority spin, and so forth. A closer look reveals that energy corrections from the majority-majority spin channel remain minuscule across the considered terms following the x axis. The majority-minority spin channel flourishes, while it contributes to E_{local} at a reduced volume but diminishes rapidly beyond the experimental volume. Conversely, the minority-minority spin channel possesses a handful of two-body operators that notably amplify their contributions to E_{local}, indicating a swift rise in electronic repulsion between specific states. The composite energy correction trajectory,

TABLE I. The BM-EOS fitted equilibrium lattice constant a_0, bulk modulus B_0, spin magnetic moment M, and its pressure derivative of ferromagnetic bcc iron out of various calculations. HF, LDA+U, and CMRT were evaluated with QUAMBO basis set in this work. LSDA and GGA [20], LDA+DMFT($U = 4.3$eV, $J = 1.0$eV) [29], LDA+G($U = 7.0$eV, $J = 1.0$eV) [35] were evaluated with the planewave basis set.

	Expt.	HF	LSDA	GGA	LDA+U	LDA+G	LDA+DMFT	CMRT
a_0 (Å)	2.87[a]	3.0	2.75	2.83	2.76	2.85	2.853	2.887
B_0 (GPa)	168.3[a]	115	247	174	207	160	168	165
M (μ_B)	2.2[a]	2.92	2.0	2.2	2.13	2.30	2.2	2.6
$-\partial \ln M/\partial P$ (10^{-4}/kBar))	2.5[b],3.2[c]		4.9[c], 4.4[d]	3.9[d]				2.85

[a]Reference [1].
[b]Reference [49].
[c]Reference [50].
[d]This work.

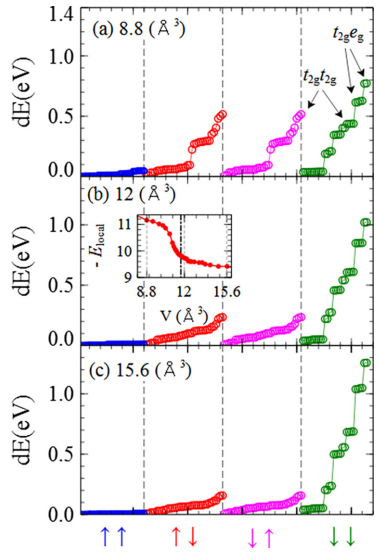

FIG. 3. The two-body energy components contributing to local energy correction as defined in Eq. (2) at three typical volumes of the bcc iron lattice. Empty circles represent each two-body energy component given by $dE = U^{\alpha\alpha\beta\beta}_{iiii}(\bar{n}_{i\alpha\sigma}\bar{n}_{i\beta\sigma'} - \langle\hat{n}_{i\alpha\sigma}\hat{n}_{i\beta\sigma'}\rangle)$ with the $U^{\alpha\alpha\beta\beta}_{iiii}$ local bare Coulomb integral matching the $\hat{n}_{i\alpha\sigma}\hat{n}_{i\beta\sigma'}$ operator, and are sorted in ascending order on the x axis for each spin-spin channel at a designated volume. Consequently, symbols located at the same x coordinate in different volumes may not represent the same operator unless explicitly indicated. Vertical dashed lines distinguish these channels with corresponding consistently colored circles. The up arrow signifies majority spin, while the down arrow indicates minority spin. Prominent local energy correction components pointed with arrows are tagged as $t_{2g}e_g$ and $t_{2g}t_{2g}$, representing local two-body operators of $\hat{n}_{t_{2g},\sigma}\hat{n}_{e_g,\sigma}$ and $\hat{n}_{t_{2g},\sigma}\hat{n}_{t'_{2g},\sigma'}$, respectively. Inset: The volume dependence of local energy correction induced by electronic correlation and expressed as $-E_{\rm local}$ in the CMRT energy expression of Eq. (1). The thick dashed vertical line there marks the experimental equilibrium volume, while the trio of dashed grid lines point out where the energy components were sampled.

presented in the inset of Fig. 3, unveils that the gains from enhanced terms in the minority-minority spin channel fail to offset the dwindling contributions from the majority-minority two-body terms.

B. Local orbital occupations and their fluctuations

A comprehensive examination of the local physics is presented in the ferromagnetic bcc iron lattice using the CMRT method. Figure 4 gives local orbital occupancies on the t_{2g} and e_g states of a $3d$ orbit at an atomic volume of 11.94 Å ^{3} (or $a = 2.88$ Å) across various *ab initio* methods. The orbital occupancies of CMRT exhibit close alignment with most methods, except for HF. Specifically, LSDA and CMRT, using the QUAMBO local orbit basis set, both yield roughly 1.3 electrons in each of the t_{2g} and e_g states. However, a notable discrepancy arises with the HF method, especially in the minority spin channel, where t_{2g} occupancy considerably exceeds that of the e_g state, suggesting a dominant role of local $3d$ energy components in the HF total energy. More details are provided in the discussion. The CMRT formalism, built upon the HF method, yields much more balanced

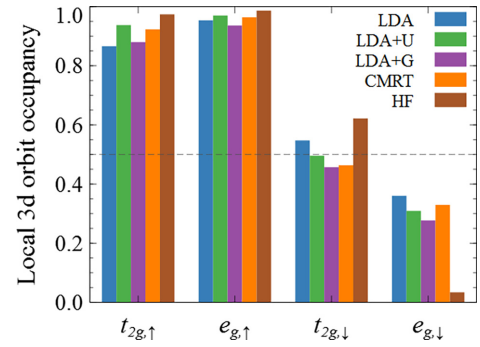

FIG. 4. Local charge occupation of the t_{2g} and e_g states within the $3d$ orbit collected from HF, CMRT, LDA + U ($U = 2.3$ eV, $J = 0.9$ eV), and LDA + G ($U = 2.5$ eV, $J = 1.2$ eV) [34]. All calculations are collected at an atomic volume of roughly 12 Å^3.

orbital occupancies between the t_{2g} and e_g states. Interestingly, while CMRT predicts a somewhat higher ordered spin magnetic moment compared to the LSDA and PBE calculations, its volume dependence resonates remarkably well with experimental measurements, as evidenced by the consistency of the pressure derivative of the logarithm of the spin magnetic moment with the data presented in Table I. This congruence underscores the CMRT formalism's strength, while maintaining the convenience of the HF method, in assimilating electronic correlation effects. It does so by meticulously renormalizing effective single-particle hoppings and rigorously treating local two-body interactions. As a result, this approach not only moderates the excessively high local spin moment observed in HF, but also achieves a more balanced distribution of electron occupancy between both states in the minority spin channel. Furthermore, it helps CMRT avoid an artifact phase transition inherent in HF, rectifying the imbalanced orbital occupancies with reduced volume, as depicted in Fig. 5.

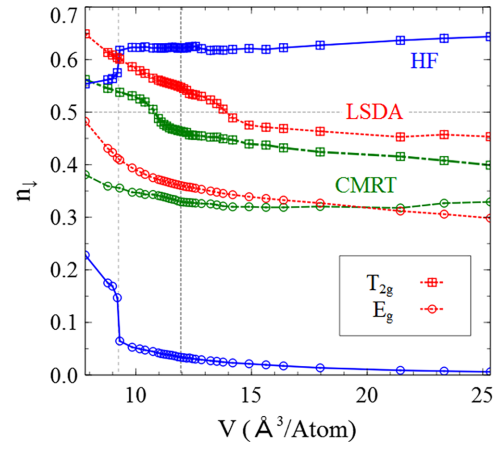

FIG. 5. Dependence of local orbital occupation on atomic volume for both the t_{2g} and e_g states in the minority spin channel of bcc iron, as assessed by LSDA, CMRT, and HF methods employing the QUAMBO basis set. The vertical dashed lines from left to right mark the sudden occupation change of HF and the experimentally determined equilibrium volume, respectively.

To delve deeper into local fluctuations, we introduce a local pseudocharge correlator as

$$\chi_{i\alpha\sigma,i\beta\sigma'} = \langle \hat{n}_{i\alpha\sigma}\hat{n}_{i\beta\sigma'}\rangle - \bar{n}_{i\alpha\sigma}\bar{n}_{i\beta\sigma'} \quad \text{for } (\alpha\sigma) \neq (\beta\sigma'). \quad (8)$$

This correlator serves as an insightful metric to gauge the electronic correlation between two electronic states, effectively capturing how one electron's presence might influence another's motion. In essence, this correlator quantifies the deviation in the likelihood of observing a specific electron pair, $\langle \hat{n}_{i\alpha\sigma}\hat{n}_{i\beta\sigma'}\rangle$, which can be thoroughly evaluated within CMRT, from a baseline uncorrelated value, $\bar{n}_{i\alpha\sigma}\bar{n}_{i\beta\sigma'}$. When the expectation value is evaluated with a single Slater determinant ground-state wave function, the result would yield the Hartree term as the baseline value, and a much smaller Fock term if the working basis set possesses the correct lattice and orbital symmetry. Thus, this correlator would nearly vanish in a noninteracting system, as expected for two electrons being uncorrelated.

Introduce local charge and spin (z component only) operators as $\hat{n}$ and $\hat{S}_z$ and we can write the local static charge and spin (z component only) fluctuations, $\chi_{\hat{n}}$ and $\chi_{\hat{S}_z}$, as

$$\hat{n} = \sum_{\alpha,\sigma} \hat{n}_{\alpha,\sigma} \Rightarrow \chi_{\hat{n}} = \langle (\hat{n} - \bar{n})^2 \rangle, \quad (9)$$

$$\hat{S}_z = \frac{1}{2}\sum_{\alpha,\sigma} \sigma \hat{n}_{\alpha,\sigma} \Rightarrow \chi_{\hat{S}_z} = \langle (\hat{S}_z - \bar{S}_z)^2 \rangle, \quad (10)$$

with α indexing a set of local orbits and $\sigma = \pm 1$ denoting majority and minority spins, respectively. A simple algebra establishes the following relationship between fluctuations and pseudocharge correlator:

$$4\chi_{\hat{S}_z} - \chi_{\hat{n}} = 4\sum_{\alpha\beta}(-\chi_{\alpha\uparrow,\beta\downarrow}). \quad (11)$$

Given a single orbit, the above equation provides a way to gain insights into local double occupancy by taking the difference between the two fluctuations.

Figure 6 compiles the spin and charge fluctuations from various sets of local orbits and highlights the dominant pseudocharge correlators. Figures 6(a) and 6(b) dissect the fluctuations within all $3d$ orbits, and within t_{2g} and e_g states, respectively. The principal variability in spin fluctuation predominantly concerns the t_{2g} states, especially at smaller lattice volumes. Figure 6(c) provides a clearer perspective on the observation by representing fluctuations for individual states. By noting that local fluctuations of the $4S$ state are not suppressible with increasing electronic correlation, we might reliably classify the $4S$ state as weakly correlated. Meanwhile, as volume increases, Fig. 6(c) suggests that the t_{2g} and e_g states exhibit weak correlation, as indicated by $\langle \hat{n}_{i\alpha\uparrow}\hat{n}_{i\alpha\downarrow}\rangle \simeq \bar{n}_{i\alpha\uparrow}\bar{n}_{i\alpha\downarrow}$ readily read out from the diminishing difference between the spin and charge fluctuations and with the help of Eq. (11). This weak correlation arises from the nearly filled $3d$ orbits in the majority spin channel. The minority spin channel in the $3d$ orbits, however, are the chief contributor to local electronic correlations. This observation stems from Fig. 3 and is corroborated by Fig. 6(d). This panel showcases $\chi_{i\alpha\sigma,i\beta\sigma'}$ adjusted by $\bar{n}_{i\alpha\sigma}\bar{n}_{i\beta\sigma'}$ to account for variations in orbital occupation within a state pair $(\alpha\sigma, \beta\sigma')$. Such an approach can compare electronic correlations across different state pairs, as is supported by two notable advantages. First, all state pairs maintain their numerical alignment at one as the noninteracting limit. Second, the visualization aptly highlights the few most significant electronic correlations and pinpoints the state pairs that generate them. These predominant correlations between t_{2g} and e_g could be the reason for their rebalanced occupations in CMRT, which are otherwise significantly skewed in the HF calculation shown in Fig. 4.

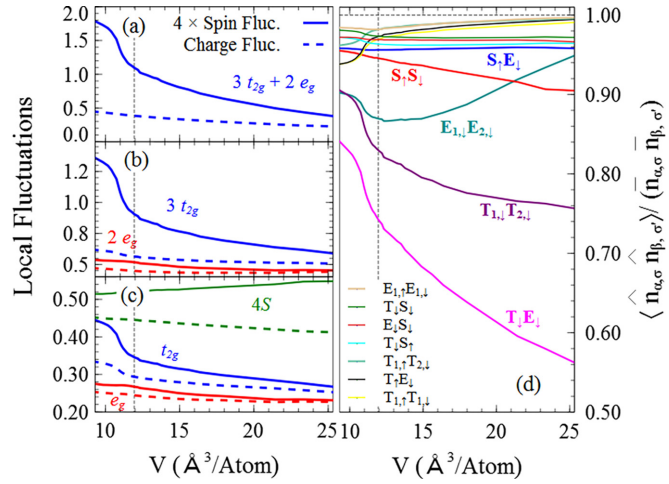

FIG. 6. Left panels show local spin and charge fluctuations with different sets of local states. Solid lines show four times spin fluctuation and dashed lines show charge fluctuation. Panel (a) selects all t_{2g} and e_g states to define the spin and charge operators; panel (b) selects all t_{2g} states as well as all e_g states, while panel (c) picks up individual $4S$, t_{2g}, and e_g states to evaluate their spin and charge fluctuations. The right panel (d) gives comparisons of $\langle \hat{n}_{\alpha\sigma}\hat{n}_{\beta\sigma'}\rangle$ normalized by $\bar{n}_{\alpha\sigma}\bar{n}_{\beta\sigma'}$ with $\bar{n}_{\alpha\sigma} = \langle \hat{n}_{\alpha\sigma}\rangle$. The first five biggest terms have their labels put near the curves with matching colors. In contrast, the rest of the terms have their labels collected at the left-bottom corner following roughly the magnitude ordering at a small lattice volume. The curves are consistently labeled with two capital letters denoting a pair of local orbits involved. Specifically, T, E, S denote t_{2g}, e_g, and $4S$ states averaged over their degenerate states, respectively. If the same state is involved in both local orbits, then each letter carries a number to distinguish whether they are the same state. For instance, $T_{1,\uparrow}T_{2,\downarrow}$ denotes $\hat{n}_{\alpha\uparrow}\hat{n}_{\beta\downarrow}$ with $\alpha, \beta \in \{t_{2g}\}$ but $\alpha \neq \beta$, while $T_{1,\uparrow}T_{1,\downarrow}$ denotes $\hat{n}_{\alpha\uparrow}\hat{n}_{\alpha\downarrow}$ for $\alpha \in \{t_{2g}\}$, which is basically the averaged double occupancy of an individual t_{2g} state. The spin index $\sigma \in \{\uparrow, \downarrow\}$ denotes majority or minority spins, respectively. In both panels, the vertical dotted lines show the CMRT equilibrium volume.

C. Normalized local charge fluctuation analysis

While the Gutzwiller renormalization prefactors for the correlated orbits shown in Fig. 7 reveal some similarity between the t_{2g} and e_g states in both spin channels, the difference might be explored through the normalized local charge fluctuation (NLCF), defined as $\chi_{\hat{n}}/\bar{n}^2$ [44]. We evaluate this metric using CMRT and HF calculations, with HF serving as the reference for electronic correlation. Notable deviations between CMRT and HF indicate additional correlations captured by CMRT. For a balanced comparison, we introduce a standardized NLCF (sNLCF). Given the noncomparability of

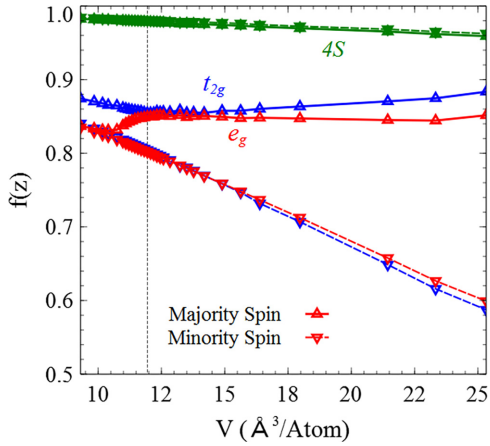

FIG. 7. Volume dependence of Gutzwiller renormalization factor $f(z_{\alpha\sigma})$ for both spin channels for selected local states. Blue curves are for t_{2g}, red for e_g, and green for $4S$ states. Solid lines with an upward triangle represent the majority spin, while dashed lines with a downward triangle represent the minority spin. The dashed vertical line indicates the CMRT equilibrium volume with the ferromagnetic bcc iron lattice.

expectation values in the NLCF definition across methods, we adjusted their range to fall between 0 and 1 in sNLCF after taking appropriate constant shifts.

Figure 8 contrasts the sNLCF values from CMRT and HF across subsets of local correlated orbits in a ferromagnetic bcc iron system. This figure presents relative charge fluctuations across different choices of orbits (rows) and spin channels (columns). The top row illustrates CMRT vs HF for all five $3d$

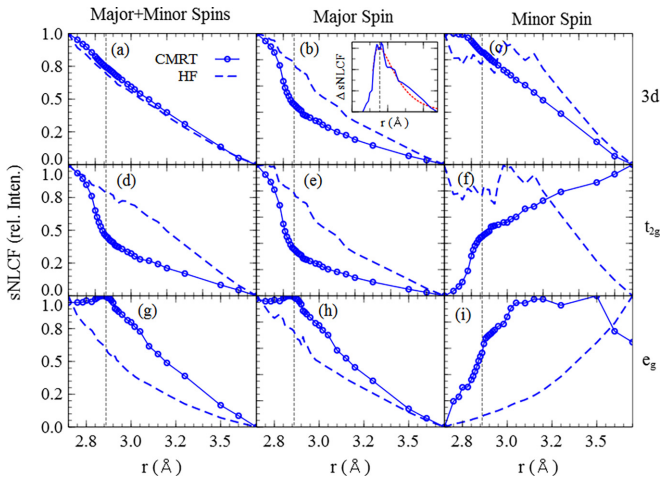

FIG. 8. sNLCF results from both HF and CMRT methods are brought side by side in the plots. Labels on the top of the figure show different spin channels of sNLCF in the columns, while labels to the right of the figure show the chosen local orbits for sNLCF calculation in each row. Specifically, $3d$ means that all $3d$ local orbitals of the prechosen spins are selected to define NLCF; t_{2g} and e_g denote that a single specific state is chosen for the sNLCF calculation. The inset in (b) shows the lattice constant dependence of the difference in sNLCF between the HF and CMRT data with the dashed red curve a smooth fit of the difference to indicate the maximum. The dashed vertical line denotes the equilibrium lattice constant determined from CMRT.

orbits, and the middle and bottom rows focus on comparisons for individual t_{2g} and e_g states, respectively. In interpreting Fig. 8, it is evident that different treatments in electronic correlation between methods yield different sNLCF behaviors. Specifically, the majority spin channel in the second column reveals HF's near-linear descent as contrasted with CMRT's well-established curvatures. CMRT either further suppresses or enhances charge fluctuations on top of HF in the t_{2g} or e_g states for a better treatment of their electronic correlations. This qualitative difference in the t_{2g} and e_g treatments supports the distinct correlation nature of both $3d$ states made in the existing literature. The curve in the inset of Fig. 8(b), resulting from the difference between HF and CMRT there, peaks near the CMRT equilibrium volume. This might suggest a predominant role of majority spin electrons in shaping the interatomic bonds and the bulk bcc lattice structure.

IV. DISCUSSION

We demonstrated that CMRT can correctly predict both the energy versus volume (E-V) and pressure versus volume (P-V) curves for the bulk bcc iron ferromagnetic phase. Furthermore, it yields an equilibrium volume and bulk modulus consistent with experimental findings, as illustrated in Fig. 2. CMRT also produced other credible physical quantities such as local orbital renormalization prefactors and orbital occupations. All these suggest that CMRT can capture the essential correlation physics inherent in the $3d$ orbits of this system. These extra correlations built into CMRT aid in redistributing the system's kinetic and potential energies, and orbital fillings. While there was analysis indicating that changes in these energy components correlate with the formation of ordered moments [34], we choose not to delve into such intricacies here, supposing that this information might be method specific. Meanwhile, CMRT predicts a local spin magnetic moment larger than experimental measurements. The local state occupations depicted in Fig. 4 reveal that HF-based CMRT still allocates more electrons to the majority spin channel than LSDA/GGA, resulting in an exaggerated local spin magnetic moment. Interestingly, local interaction enhanced LSDA methods, such as DFT + U and DFT + G, display similar local state occupations as CMRT, even though they stem from distinct theoretical backgrounds, namely, LSDA and HF.

The local $3d$ occupation in HF significantly skews towards t_{2g} states in the minority spin channel compared to the other methods, as depicted in Fig. 4. Generally speaking, a preferred occupation on t_{2g} over e_g is consistent with the cubic crystal field splitting of $3d$ orbits [51]. But, this skewness in the HF calculation seems excessively pronounced. Insight into this phenomenon may be gleaned by examining a simplified model of an isolated atom. This model replicates the local electron filling pattern observed in the ferromagnetic iron state, i.e., nearly fully filled $3d$ orbits in the majority spin channel and a predetermined number of $3d$ electrons in the minority spin channel. We closely observe $\hat{n}_{\alpha\sigma}\hat{n}_{\beta\sigma'}$-type two-body operators, with $\alpha, \beta \in \{t_{2g}, e_g\}$, which are dominant in the atomic Hamiltonian and possess very close Coulomb energy coefficients. The classical Coulomb potential energy pertinent to these operators is expressed

as follows:

$$E_p \propto C_3^2 \bar{n}_{t_{2g},\downarrow}\bar{n}_{t_{2g},\downarrow} + 6\bar{n}_{t_{2g},\downarrow}\bar{n}_{e_g,\downarrow} + C_2^2 \bar{n}_{e_g,\downarrow}\bar{n}_{e_g,\downarrow}, \quad (12)$$

which might as well be thought of as a mean-field decomposition on $\hat{n}_{\alpha\sigma}\hat{n}_{\beta\sigma'}$, but having the Fock terms dropped as quantum effects. In this equation, $\bar{n}_{t_{2g}(e_g),\downarrow}$ represents local orbital occupation in a t_{2g} or e_g state in the minority spin channel, while C_n^m is the standard binomial coefficient. Simple algebraic manipulation reveals three notable cases [52]. Two extremes, $(\bar{n}_{t_{2g},\downarrow}, 0)$ and $(0, \bar{n}_{e_g,\downarrow})$, represent charge-bounded local minima separated by a third potential energy maximum, which actually corresponds to the physically relevant case holding equal occupation in all $3d$ orbits for an isolated atom with nearly degenerate orbits. Given this scenario, it is reasonable to hypothesize that the HF solution likely corresponds to one of the two extreme cases in an effort to minimize the local potential energy. Confirmation of this hypothesis is obtained by applying HF to the local atomic Hamiltonian constructed at a reference site on the bcc iron lattice with a unit cell volume of 25 Å ^{3}(or $a_0 = 3.7$ Å). The HF approach, contingent on specific initial orbital occupations, readily converges to one of the two extreme cases with vanishing occupation in either type of the $3d$ states. Comparing these solutions to the actual HF solution for the bcc iron lattice reveals that the extra nonlocal hoppings and interactions left out of the local atomic Hamiltonian help promote electrons to empty states instead of redistributing them among the occupied states. With local correlation effects incorporated in the HF framework to establish CMRT—which effectively reduces the local Coulomb interaction as showcased in Fig. 6—a greater number of electrons continue to transit into the empty $3d$ states. This results in a more balanced electron occupation among the $3d$ states, which would otherwise be energetically discouraged by a local energy Hamiltonian as seen through HF.

Based on the classical potential energy depicted in Eq. (12) and the different orbital occupations between HF and CMRT, two key observations are made. First, local correlation is crucial in reestablishing the correct physical picture in the bcc iron lattice with CMRT. While correlation may reduce the nonlocal energy components through Gutzwiller renormalization, the overarching effect is an enhanced nonlocal effect, ensuring a steady electron flow into empty $3d$ states. Second, integrating the exchange-correlation functional into DFT markedly enhances its efficacy, as evidenced here by a correct depiction of many physical properties of the bcc iron lattice. Nevertheless, the similarity in electronic behaviors yielded by both HF and the classical Coulomb repulsion positions HF to be a benchmark methodology in comparing the electronic correlation effect treatment, which is purely quantum in nature. These insights might be instrumental in resolving an inconsistent statement made in a QSGW calculation [25] stating that local physics is irrelevant for describing a bcc iron lattice by taking DFT as its reference.

The local correlated energy, E_{local}, as defined in Eq. (2), encapsulates the effect of correlation on the electronic Coulomb interaction energy. When this quantity is subtracted from the CMRT total energy, the equilibrium lattice volume shifts to approximately that of the HF equilibrium volume. This alignment might seem coincidental, given that CMRT and HF converge to distinct ground states with varying orbital occupations in the minority spin channel. Nevertheless, this shifting trend underscores the significance of accurately addressing correlation effects for a precise depiction of a physical system. Segmenting E_{local} into two-body energy components reveals a competition of correlation energy across different spin-spin channels, as illustrated in Fig. 3. The dominant roles of the electronic correlation of the t_{2g} and e_g states in the minority spin channel are further highlighted in Fig. 6. Concurrently, these figures emphasize the weak correlation present within the majority spin channel of these states—a perspective somewhat at odds with the insights from $f(z)$ in Fig. 7. One possible explanation is that $\chi_{\alpha\sigma,\beta\sigma'}$ expresses the magnitude of static correlation for two electrons in a system's final state, which emerges after the culmination of all inherent physical screening and damping effects. In contrast, $f(z)$ may be dynamically significant for individual orbits, facilitating quasiparticle renormalization and giving rise to the needed screening and damping effects on electronic motion. Thus, while $\chi_{\alpha\sigma,\beta\sigma'}$ might quantify how easy two electrons approach each other, a view on correlation from a potential perspective, its numerical connection with the Gutzwiller renormalization factor $f(z)$ expressing how much single-particle motion is affected, a view on correlation from a kinetic perspective, is uncertain. Such an interpretation might further help reconcile a statement made in a LDA + DMFT calculation claiming a strong correlation effect in the majority spin channel [37]. The claim was made through self-energy, which is intricately connected with the Gutzwiller renormalization prefactor [39].

Analysis of local fluctuations and pseudocharge correlators suggested distinct correlation patterns for $3d$ orbits in the majority and minority spin channels. A closer look at pseudocharge correlators associated with t_{2g} and e_g states in Fig. 6 indicates that both orbits exhibit significant interactions within and between them in the minority spin channel, but without qualitative differences. Hence, categorizing t_{2g} and e_g states as purely itinerant and localized states or attributing them different electronic characteristics [9] is not wholly corroborated by our findings. Subsequent analysis exploring local fluctuation was carried out. While NLCF can be insightful for analyzing electronic localization in strongly correlated systems, as done in Refs. [43,44], it did not yield anything substantial for the bulk bcc iron system. This aligns with the notion that localization-delocalization dynamics are not a primary concern in this system. On the other hand, by accessing the standardized NLCF for $3d$ orbits and contrasting them with HF computations, it becomes evident that t_{2g} and e_g states have a subtle distinction in the majority spin channel. As shown in Figs. 8(e) and 8(h), while they almost retain their local orbit occupations, their local charge fluctuations are modulated in opposing directions to optimize electronic correlation energy for the CMRT ground state. The profound difference in the behaviors of the t_{2g} and e_g states within the majority spin channel warrants further investigation.

V. SUMMARY

In this study, we expanded the capabilities of CMRT, an entirely *ab initio* approach for correlated electron systems, to accommodate magnetization by facilitating straightforward

spin polarization within the system. Unlike LDA + DMFT and LDA + G, CMRT does not require Hubbard U and Hund's J parameters, instead directly utilizing bare Coulomb interactions. Moreover, CMRT does not have the double-counting issues. These unique features are crucial for a predictive theory and are a primary motivation for this development. Meanwhile, CMRT offers a computationally efficient and faster alternative to LDA + DMFT, akin to LDA + G in terms of the impurity solver. We benchmarked this formalism against the established ferromagnetic system of the bulk bcc Fe lattice. Interestingly, we found that utilizing spin-independent sum rule energy coefficients yields the most accurate results in the CMRT total-energy computation. This observation is in harmony with a raw *ab initio* Hamiltonian employing spin-independent energy parameters. We charted the CMRT E-V curve for this system and derived equilibrium attributes such as volume and bulk modulus. These values align well with experimental data and compare positively to other *ab initio* methodologies. Furthermore, our constructed P-V curve not only mirrors experimental results, but also demonstrates better concordance than GGA predictions. Diving deeper, we extensively examined local physical metrics, including local orbit occupation, local spin and charge fluctuations, and local correlation effects analyzed with new measures introduced in this study. Our findings pinpointed the primary correlation impact to the 3d orbits within the minority spin channel and highlighted subtle distinctions between the t_{2g} and e_g states. Towards the majority spin channel, while it exhibits weak correlation, the behaviors of t_{2g} and e_g can be notably different. Such a difference might hinge on the method used, and its physical implications remain unclear.

ACKNOWLEDGMENTS

We would like to thank F. Zhang and J. H. Zhang for valuable discussions. This work was supported by the U.S. Department of Energy (DOE), Office of Science, Basic Energy Sciences, Materials Science and Engineering Division, including the computer time support from the National Energy Research Scientific Computing Center (NERSC) in Berkeley, CA. The research was performed at Ames National Laboratory, which is operated for the U.S. DOE by Iowa State University under Contract No. DEAC02-07CH11358.

[1] C. Kittel, *Introduction to Solid State Physics*, 8th ed. (Wiley, New York, 2004).

[2] K. Kanematsu, S. Misawa, M. Shiga, H. Wada, and H. P. J. Wijn, *Landolt-Bornstein: Numerical Data and Functional Relationships in Science and Technology*, Group III: Condensed Matter Vol. 32; Magnetic Properties of Metals, Supplement to Vol. 19, Subvol. A, 3d, 4d and 5d Elements, Alloys and Compounds (Springer, New York, 2017).

[3] E. Antonides, E. C. Jose, and G. A. Sewatzky, Lmm auger spectra of Cu, Zn, Ga, and Ge. I. Transition probabilities, term splittings, and effective Coulomb interaction, Phys. Rev. B **15**, 1669 (1977).

[4] D. Chandesris, J. Lecante, and Y. Petroff, Two-electron resonances in transition metals, Phys. Rev. B **27**, 2630 (1983).

[5] L. I. Yin, T. Tsang, and I. Adler, Electron delocalization and the characterization of the L_3MM auger spectra of 3d transition metals, Phys. Rev. B **15**, 2974 (1977).

[6] E. Şaşıoğlu, C. Friedrich, and S. Blügel, Effective Coulomb interaction in transition metals from constrained random-phase approximation, Phys. Rev. B **83**, 121101(R) (2011).

[7] A. Gutiérrez and M. F. López, Angle-resolved resonant photoemission at the M_{III} absorption threshold of Co and Fe metal, Phys. Rev. B **56**, 1111 (1997).

[8] E. P. Wohlfarth, *Iron, Cobalt and Nickel* (North-Holland, Amsterdam, 1980), Vol. 1, pp. 1.

[9] A. A. Katanin, A. I. Poteryaev, A. V. Efremov, A. O. Shorikov, S. L. Skornyakov, M. A. Korotin, and V. I. Anisimov, Orbital-selective formation of local moments in α-iron: First-principles route to an effective model, Phys. Rev. B **81**, 045117 (2010).

[10] D. J. Singh, W. E. Pickett, and H. Krakauer, Gradient-corrected density functionals: Full-potential calculations for iron, Phys. Rev. B **43**, 11628 (1991).

[11] J. Staunton, B. L. Györffy, A. J. Pindor, G. M. Stocks, and H. Winter, The "disordered local moment" picture of itinerant magnetism at finite temperatures, J. Magn. Magn. Mater. **45**, 15 (1984).

[12] M. B. Stearns, On the origin of ferromagnetism and the hyperfine fields in Fe, Co, and Ni, Phys. Rev. B **8**, 4383 (1973).

[13] P. Hohenberg and W. Kohn, Inhomogeneous electron gas, Phys. Rev. **136**, B864 (1964).

[14] W. Kohn and L. J. Sham, Self-consistent equations including exchange and correlation effects, Phys. Rev. **140**, A1133 (1965).

[15] U von Barth and L. Hedin, A local exchange-correlation potential for the spin polarized case. I, J. Phys. C: Solid State Phys. **5**, 1629 (1972).

[16] John P. Perdew and Y. Wang, Accurate and simple analytic representation of the electron-gas correlation energy, Phys. Rev. B **45**, 13244 (1992).

[17] C. S. Wang, B. M. Klein, and H. Krakauer, Theory of magnetic and structural ordering in iron, Phys. Rev. Lett. **54**, 1852 (1985).

[18] J. P. Perdew, K. Burke, and M. Ernzerhof, Generalized gradient approximation made simple, Phys. Rev. Lett., **77**, 3865 (1996).

[19] L. Stixrude, R. E. Cohen, and D. J. Singh, Iron at high pressure: Linearized-augmented-plane-wave computations in the generalized-gradient approximation, Phys. Rev. B **50**, 6442 (1994).

[20] G. Kresse and D. Joubert, From ultrasoft pseudopotentials to the projector augmented-wave method, Phys. Rev. B **59**, 1758 (1999).

[21] J. Schäfer, M. Hoinkis, E. Rotenberg, P. Blaha, and R. Claessen, Fermi surface and electron correlation effects of ferromagnetic iron, Phys. Rev. B **72**, 155115 (2005).

[22] O. Gunnarsson, Band model for magnetism of transition metals in the spin-density-functional formalism, J. Phys. F: Met. Phys. **6**, 587 (1976).
[23] A. Yamasaki and T. Fujiwara, Electronic structure of transition metals Fe, Ni and Cu in the GW approximation, J. Phys. Soc. Jpn. **72**, 607 (2003).
[24] T. Kotani, M. van Schilfgaarde, and S. V. Faleev, Quasiparticle self-consistent GW method: A basis for the independent-particle approximation, Phys. Rev. B **76**, 165106 (2007).
[25] L. Sponza, P. Pisanti, A. Vishina, D. Pashov, C. Weber, M. van Schilfgaarde, S. Acharya, J. Vidal, and G. Kotliar, Self-energies in itinerant magnets: A focus on Fe and Ni, Phys. Rev. B **95**, 041112(R) (2017).
[26] C. Barreteau, M.-C. Desjonquères, A. M. Oleś, and D. Spanjaard, Effects of intersite Coulomb interactions on ferromagnetism: Application to Fe, Co, and Ni, Phys. Rev. B **69**, 064432 (2004).
[27] A. S. Belozerov and V. I. Anisimov, Coulomb interaction parameters in bcc iron: An LDA+DMFT study, J. Phys.: Condens. Matter **26**, 375601 (2014).
[28] A. I. Lichtenstein, M. I. Katsnelson, and G. Kotliar, Finite-temperature magnetism of transition metals: An *ab initio* dynamical mean-field theory, Phys. Rev. Lett. **87**, 067205 (2001).
[29] L. V. Pourovskii, J. Mravlje, M. Ferrero, O. Parcollet, and I. A. Abrikosov, Impact of electronic correlations on the equation of state and transport in ϵ-Fe, Phys. Rev. B **90**, 155120 (2014).
[30] J. Sánchez-Barriga, J. Fink, V. Boni, I. Di Marco, J. Braun, J. Minár, A. Varykhalov, O. Rader, V. Bellini, F. Manghi, H. Ebert, M. I. Katsnelson, A. I. Lichtenstein, O. Eriksson, W. Eberhardt, and H. A. Dürr, Strength of correlation effects in the electronic structure of iron, Phys. Rev. Lett. **103**, 267203 (2009).
[31] M. Cococcioni and S. de Gironcoli, Linear response approach to the calculation of the effective interaction parameters in the LDA + U method, Phys. Rev. B **71**, 035105 (2005).
[32] V. I. Anisimov, A. S. Belozerov, A. I. Poteryaev, and I. Leonov, Rotationally invariant exchange interaction: The case of paramagnetic iron, Phys. Rev. B **86**, 035152 (2012).
[33] M. I. Katsnelson and A. I. Lichtenstein, LDA + + approach to the electronic structure of magnets: Correlation effects in iron, J. Phys.: Condens. Matter **11**, 1037 (1999).
[34] G. Borghi, M. Fabrizio, and E. Tosatti, Gutzwiller electronic structure calculations applied to transition metals: Kinetic energy gain with ferromagnetic order in bcc Fe, Phys. Rev. B **90**, 125102 (2014).
[35] X. Y. Deng, X. Dai, and Z. Fang, LDA+Gutzwiller method for correlated electron systems, Europhys. Lett. **83**, 37008 (2008).
[36] T. Schickling, J. Bünemann, F. Gebhard, and L. Boeri, Quasiparticle bands and structural phase transition of iron from Gutzwiller density-functional theory, Phys. Rev. B **93**, 205151 (2016).
[37] A. Grechnev, I. Di Marco, M. I. Katsnelson, A. I. Lichtenstein, J. Wills, and O. Eriksson, Theory of bulk and surface quasiparticle spectra for Fe, Co, and Ni, Phys. Rev. B **76**, 035107 (2007).
[38] Y. O. Kvashnin, O. Grånäs, I. Di Marco, M. I. Katsnelson, A. I. Lichtenstein, and O. Eriksson, Exchange parameters of strongly correlated materials: Extraction from spin-polarized density functional theory plus dynamical mean-field theory, Phys. Rev. B **91**, 125133 (2015).
[39] N. Lanatà, Y. Yao, C.-Z. Wang, K.-M. Ho, and G. Kotliar, Phase diagram and electronic structure of praseodymium and plutonium, Phys. Rev. X **5**, 011008 (2015).
[40] C. Liu, J. Liu, Y. X. Yao, P. Wu, C. Z. Wang, and K. M. Ho, Correlation matrix renormalization theory: Improving accuracy with two-electron density-matrix sum rules, J. Chem. Theory Comput. **12**, 4806 (2016).
[41] J. Liu, X. Zhao, Y. Yao, C.-Z. Wang, and K.-M. Ho, Correlation matrix renormalization theory in multiband lattice systems, J. Phys.: Condens. Matter **33**, 095902 (2021).
[42] X. Zhao, J. Liu, Y.-X. Yao, C.-Z. Wang, and K.-M. Ho, Phys. Rev. B **97**, 075142 (2018).
[43] J. Liu, Y. Yao, J. Zhang, V. Antropov, K.-M. Ho, and C.-Z. Wang, *Ab initio* study on fcc Pr with correlation matrix renormalization theory, Phys. Rev. B **106**, 205124 (2022).
[44] J. Liu, Y. Yao, J. Zhang, K.-M. Ho, and C.-Z. Wang, Role of Coulomb interaction in the phase formation of fcc Ce: Correlation matrix renormalization theory, Phys. Rev. B **104**, L081113 (2021).
[45] G. Kresse and J. Furthmüller, Efficient iterative schemes for *ab initio* total-energy calculations using a plane-wave basis set, Phys. Rev. B **54**, 11169 (1996).
[46] X. Qian, J. Li, L. Qi, C.-Z. Wang, T.-L. Chan, Y.-X. Yao, K.-M. Ho, and S. Yip, Quasiatomic orbitals for *ab initio* tight-binding analysis, Phys. Rev. B **78**, 245112 (2008).
[47] F. D. Murnaghan, The compressibility of media under extreme pressures, Proc. Natl. Acad. Sci. USA **30**, 244 (1944).
[48] A. Dewaele, C. Denoual, S. Anzellini, F. Occelli, M. Mezouar, P. Cordier, S. Merkel, M. Véron, and E. Rausch, Mechanism of the $\alpha - \epsilon$ phase transformation in iron, Phys. Rev. B **91**, 174105 (2015).
[49] J. Madsen, O. K. Andersen, U. K. Poulsen, and O. Jepsen, Canonical band theory of the volume and structure dependence of the iron magnetic moment, AIP Conf. Proc. **29**, 327 (1976).
[50] J. F. Janak and A. R. Williams, Giant internal magnetic pressure and compressibility anomalies, Phys. Rev. B **14**, 4199 (1976).
[51] S. Blundell, *Magnetism in Condensed Matter* (Oxford University Press, Oxford, UK, 2001).
[52] By assuming n to be the initial charge in t_{2g} and supposing a subsequent change of x to produce $3x/2$ charge in the e_g states, Eq. (12) can be expressed in terms of x. Setting the derivative of Eq. (12) to zero yields the physically relevant solution, which is, however, an energy maximum. Note, also, that x is bounded between 0 and n, which correspond to the two extreme cases.